Journal of
Synchrotron
Radiation

ISSN 0909-0495

Received 17 February 2010
Accepted 7 May 2010

Fast-scanning high-flux microprobe for biological X-ray fluorescence microscopy and microXAS

R. A. Barrea,[a]* D. Gore,[a] N. Kujala,[a] C. Karanfil,[b] S. Kozyrenko,[a] R. Heurich,[a] M. Vukonich,[a] R. Huang,[c] T. Paunesku,[d] G. Woloschak[d] and T. C. Irving[a]

[a]The Biophysics Collaborative Access Team (BioCAT), Department of Biological, Chemical and Physical Sciences, Illinois Institute of Technology, Chicago, IL 60616, USA, [b]Physics Department, Faculty of Arts and Sciences, Mugla University, Kotekli-Mugla 48187, Turkey, [c]IMCA-CAT, Hauptman-Woodward Institute, Buffalo, NY 14203, USA, and [d]Departments of Radiation Oncology and Radiology, Northwestern University, Feinberg School of Medicine, Chicago, IL 60611, USA. E-mail: rbarrea@iit.edu

There is a growing interest in the biomedical community in obtaining information concerning the distribution and local chemical environment of metals in tissues and cells. Recently, biological X-ray fluorescence microscopy (XFM) has emerged as the tool of choice to address these questions. A fast-scanning high-flux X-ray microprobe, built around a recently commissioned pair of 200 mm-long Rh-coated silicon Kirkpatrick–Baez mirrors, has been constructed at BioCAT beamline 18ID at the Advanced Photon Source. The new optical system delivers a flux of 1.3×10^{12} photons s^{-1} into a minimum focal spot size of $\sim$3–5 μm FWHM. A set of Si drift detectors and bent Laue crystal analyzers may be used in combination with standard ionization chambers for X-ray fluorescence measurements. BioCAT's scanning software allows fast continuous scans to be performed while acquiring and storing full multichannel analyzer spectra per pixel on-the-fly with minimal overhead time (<20 ms per pixel). Together, the high-flux X-ray microbeam and the rapid-scanning capabilities of the BioCAT beamline allow the collection of XFM and micro X-ray absorption spectroscopy (microXAS) measurements from as many as 48 tissue sections per day. This paper reports the commissioning results of the new instrument with representative XFM and microXAS results from tissue samples.

© 2010 International Union of Crystallography
Printed in Singapore – all rights reserved

Keywords: synchrotron X-ray imaging; microprobe; microarrays; microXAS; microspectroscopy; biological samples; tissues.

1. Introduction

Metals are actively involved in many biological functions and their dysregulation can be associated with various human ailments such as neuro-degenerative diseases and cancer. There is a growing interest in the biomedical community in obtaining information concerning the distribution of metals in tissues and cells (Paunesku *et al.*, 2006, 2009). Knowledge of the local chemical environment of these metals is also important in understanding their function in metabolism in these systems (Barrea, Chen *et al.*, 2009).

Recently, biological X-ray fluorescence microscopy (XFM) has emerged as the tool of choice to address these questions. XFM is, compared with competing approaches, a relatively non-destructive technique, an essential feature for spectroscopy studies, which can provide simultaneous detection and quantization of metals that are present in thin tissue sections or single cells with very high sensitivity. Biological systems, tissues and cells are an especially challenging target of XFM studies because the elements of interest are commonly found in very low concentrations and they show a high degree of sample-to-sample variability. Therefore, X-ray fluorescence is the preferred detection mode for mapping and microXAS (micro X-ray absorption spectroscopy) experiments.

XFM is a potentially potent tool for studying the metal composition and distribution in different tissues in so-called tissue microarrays that have recently become commercially available (Farquharson *et al.*, 2007). Tissue arrays derive from a wide variety of organs and typically include normal, malignant or metastatic samples allowing the investigator to discover and validate the potential biomarkers for diagnostics and therapeutics. In order to realise the potential of using metal distribution as a biomarker, a high-performance and high-throughput XFM instrument has to be used in order to

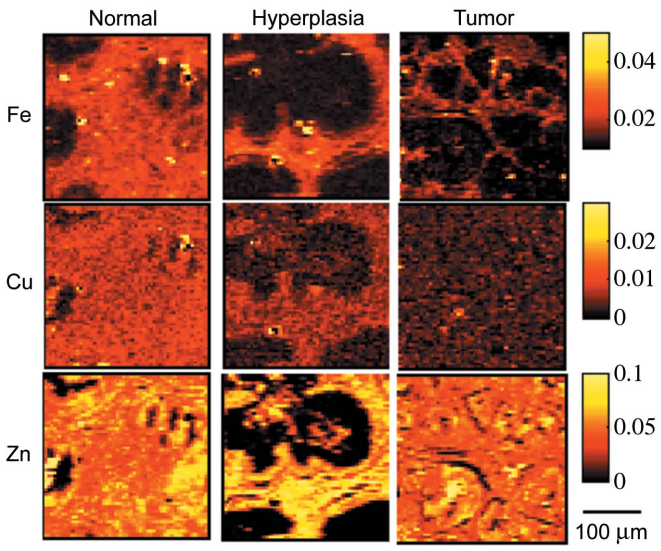

Figure 1
Examples of elemental mapping of microarray tissue sections of normal prostate tissue (adjacent to tumor), hyperplasia prostate tissue and tumor prostate tissue. The acquisition time per pixel was 0.1 s, with 12 keV incident energy. Each map contains 3700 pixels. The calibrated elemental concentrations of Fe, Cu and Zn in µg cm^{-2} are represented by the color code. Each pixel in these maps represents 5 µm × 5 µm area.

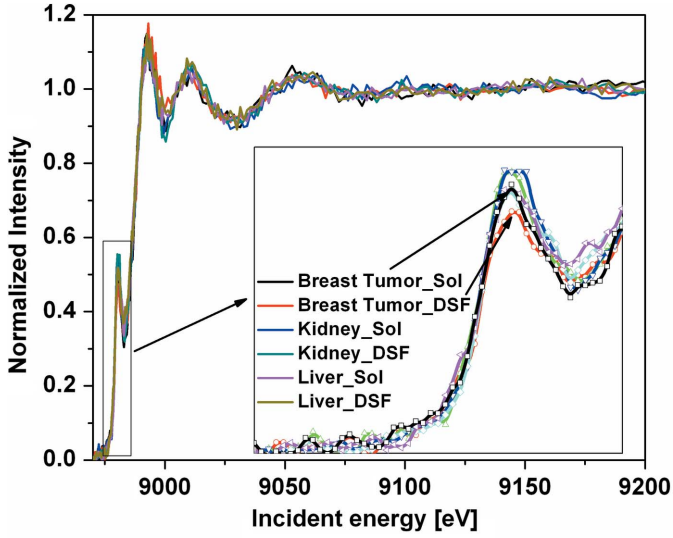

Figure 2
Cu *K*-edge microXANES from untreated and disulfiram (DSF)-treated breast tumor tissue. Normal kidney and liver tissue (from the same animals: DSF-treated and untreated) were also measured. The pre-edge peak at 8930 eV indicates a predominant Cu(I) status in all cases. There is a small but noticeable drop in intensity of the pre-edge peak in DSF-treated tumor compared with untreated tumor and to liver and kidney tissues (solvent and DSF-treated). This change suggests that DSF interacted actively and selectively with Cu tumor cells. Kidney and liver tissue spectra show no variation, suggesting DSF does not interact with Cu in normal tissue.

obtain high-quality data from the large number of individual samples in such arrays in a reasonable period of time (Figs. 1 and 2).

Third-generation synchrotron facilities are ideal for generating X-ray microbeams because of their very small source sizes and sufficient incident X-ray flux to be useful for biological studies. XFM studies can be performed at different resolution scales; micrometer resolution is optimal for tissue sections typically 10–30 µm thick (Barrea, Chen *et al.*, 2009), whereas submicrometer resolution is needed to study subcellular structures (Finney *et al.*, 2007). In principle, a single instrument cannot cover the whole range of resolutions with optimum performance. These different length scales require specialized instrumentation capable of delivering X-ray beams with the characteristics needed for these types of experiments. A number of synchrotron beamlines optimized for different imaging resolutions have been constructed or are under construction around the world for X-ray microscopy applications (Susini *et al.* 2002; Suzuki *et al.*, 2007; Heald *et al.*, 2007; Somogyi *et al.*, 2005; von Bohlen *et al.*, 2007; Marcus *et al.*, 2004; Paterson *et al.*, 2007; Barrea *et al.*, 2006).

The Biophysics Collaborative Access Team beamline (BioCAT), located at the Advanced Photon Source (APS), Argonne National Laboratory (ANL), is an undulator-based high-performance instrument designed for and dedicated to the study of partially ordered and disordered biological materials, operated as an NIH biotechnology research resource since 1997 (Fischetti *et al.*, 2004; Barrea *et al.*, 2005). Microbeam capabilities were added to the BioCAT beamline in 2005 for XFM, microXAS and microdiffraction studies of biological samples (Barrea *et al.*, 2006). The BioCAT microprobe has recently been upgraded in order to provide a high-flux microbeam with improved fast-scanning capabilities for elemental imaging and microXAS experiments on large-area tissue sections under both room- and low-temperature conditions. The microprobe also comprises highly efficient fluorescence detectors and proper sample handling hardware and software in order to achieve the throughput required for biological studies. This paper reports on the commissioning of the new Kirkpatrick–Baez mirror system, improvements of the fast-scanning software, and some results of X-ray fluorescence mapping of prostate tissue microarray samples and microXAS measurements on breast tumor tissue samples. The commercial availability of microarray tissue samples, combined with the BioCAT microprobe, provides an unprecedented opportunity for studies of metal metabolism in relationship to a wide variety of human diseases.

2. Instrumentation

2.1. Beamline and microprobe optics

The main components of the BioCAT undulator beamline 18ID comprise an APS undulator type 'A', a sagittal-bending double-crystal Si(111) monochromator and a 600 mm-long bimorph mirror for vertically focusing and harmonic rejection. The photon flux delivered by the unfocused beam (1.0 mm and 2.0 mm vertical and horizontal size, respectively) is 2.23 × 10^{13} photons s^{-1} at 12 keV. Additional details of the beamline optics can be found elsewhere (Fischetti *et al.*, 2004) (see Table 1).

Table 1
Main parameters of the BioCAT beamline and microprobe.

Source	3.3 undulator A	Source size	Vertical: 14.9 μm; horizontal: 255 μm
Monochromator type	Si(111)	Flux (photons s^{-1})	2×10^{13} at 10 keV
Energy range	3.5–35 keV	Resolution ($\Delta E/E$)	1×10^{-4}
Beam size (H × V)	Unfocused: 2 mm × 1 mm	KB mirrors focal distance	Vertical: 420 mm; horizontal: 220 mm
Beam size (H × V)	Focused: 5 μm × 5 μm	Demagnification	Vertical: 166:1; horizontal: 318:1
Microbeam flux	1.2×10^{12} at 12 keV and 9 keV	Detectors	Ion chambers; SDD Ketek 80 mm^2; BCLA

For production of microbeams, the beamline optics is supplemented by a Kirkpatrick–Baez mirror bender system (KB system) of the University of Chicago design (Eng *et al.*, 1998) with two Rh-coated silicon mirrors each 200 mm-long. Focal lengths of the horizontal and vertical KB mirrors are 220 mm and 420 mm, respectively. The bender system relies on high-precision Newport stages to provide the four required degrees of freedom per mirror: translation, tilt/rotation and upstream and downstream bending. These motorized stages are controlled by BioCAT's main control EPICS-based system. The bender system is mounted inside a Plexiglas box and filled with flowing He to keep the mirror's surfaces clean and extend their lifetime. The incoming beam is defined by a set of slits located immediately upstream of the mirror box while a 100 μm-diameter aperture downstream of the mirrors (mounted on motorized *XY* stages) acts as a guard. The whole system is mounted on a remotely controllable table that is located at the end of the experimental hutch D, 70 m downstream from the undulator source, allowing for maximum demagnification of the source (see Table 1). A layout of the beamline and microprobe set-up can be found elsewhere (Barrea *et al.*, 2006).

A 0.1 mm-thick $CdWO_4$ fluorescence screen and a CCD Hitachi HV-C20 color camera using an infinity optical system with a set of CFV-2/3/4 lenses are used during the focusing process. This system allows a reference spot to be defined for sample alignment and positioning. Beam size is determined by measuring the Ni $K\alpha$ fluorescence emission of a Ni thin film scanned across the X-ray beam (knife-edge scans). Alternatively, the beam profile can be determined using a Cool Snap monochrome camera model HQ attached to 5×/10× Zeiss objective lens and a YAG:Ce scintillator crystal (1.3 μm × 1.3 μm effective pixel size).

2.2. Pre-focusing capabilities

For most XFM microprobe applications the microbeam flux delivered by the KB mirrors is sufficient to excite the 10–20 μm-thick tissue samples and provide sufficient fluorescence signal to be detected in the time it is illuminated. In some cases though, it is desirable to count with higher photon flux, delivered onto the sample. This is accomplished by pre-focusing the X-ray beam by using the main beamline optics to generate a secondary source for the microprobe optics. Horizontal prefocusing alone increases the flux delivered three-fold. This increase is achieved at the expense of degrading the minimal focal spot size, from 5 μm to 15 μm FWHM in the horizontal direction (Huang *et al.*, 2010). The total flux density ($\sim 4.0 \times 10^{10}$ photons s^{-1} μm^{-2}) remains almost unaltered so the fluorescence signal is proportionately the same from the ∼three-fold large pixels. This mode of operation can be helpful when metal concentrations are particularly low or when a relatively large number of samples need to be screened quickly and the maximum spatial resolution requirements may be relaxed. At BioCAT, horizontal prefocusing is performed using the sagittal bending of the monochromator second crystal. These prefocusing conditions can be set up with minimum effort and require no modifications of the non-prefocused configuration. An alternative set-up for high-flux XFM applications, using a single-bounce capillary as the focusing optics, has been recently tested at BioCAT (Barrea, Huang *et al.*, 2009). Although this alternative set-up showed very good performance, it is not the standard configuration used for microbeam applications.

2.3. Sample handling and positioning

Sample positioning is performed by a set of high-precision (0.1 μm resolution) *XYZ* motorized Newport UTM25PE stages. For room-temperature measurements, custom-designed sample holders [that comply with ANL biosafety levels 1 (BSL1) and 2 (BSL2) regulations] are available. BSL1 sample holders consist of acrylic frames that provide support to thin polymer films used as sample substrates. BSL2 compatible sample holders, also made of acrylic, provide a sealed environment for samples with two removable windows that prevent contact with the tissue sections by the operator while allowing exposure of the sample to the X-ray microbeam. Both sets of holders can support up to eight different tissue sections mounted in separate compartments to avoid cross-contamination between samples. Two Linkam cryostages, model BCS 196 and its motorized version, model L-MDS600, are available for low-temperature experiments. In this case, samples are mounted on custom-designed copper holders with silicon nitride windows in order to ensure good thermal contact between the cryostage cold finger and the sample surface. A set of calibrated thin films purchased from Calmetrics are used for quantization of XFM measurements.

2.4. Detectors

Two silicon drift detectors (SDDs) are available at BioCAT: a 10 mm^2 and an 80 mm^2 active area detector, both with energy resolution of 170 eV at the Mn $K\alpha$ line. The small area detector has a thin Moxtek Ap3.3 polymer window that allows low-energy X-ray photons from light elements to be measured. Owing to its sensitivity to external light it requires a dark environment for proper operation. The 80 mm^2 area detector with a 25 μm-thick Be window is most commonly

used, especially when a large solid angle is required to increase the total count rate. Its efficiency allows the detection of fluorescence emission of elements from potassium to heavy elements. SDD detectors are typically located 60 mm away from the sample position. This distance can easily be modified using motorized stages in order to reduce or increase the overall count rate.

The fluorescence signal is collected and analyzed by two digital Saturn DXP spectrometers (XIA) that can handle up to 700000 counts s^{-1} with very good stability, although showing a large deviation from linearity at very high count rates. To avoid posterior corrections to the data collected, count rates are maintained below 50 kcounts s^{-1} whenever possible either by attenuating the beam using aluminium filters or moving the detector away to reduce the sample–detector solid angle. This practice also reduces the fluorescence signal from the sample with the consequent increase in acquisition time.

There are some cases where the intensity of the scattering signal is strong enough to mask the fluorescence signal from the sample, introducing a large background signal and sometimes saturating the solid-state detector. Bent crystal Laue analyzers (BCLAs) are alternative detection systems for these special and very limited cases. They cover absorption edges from Fe to Zn (Zhong *et al.*, 1999; Kropf *et al.*, 2003, 2005). These analyzers offer a high background rejection and high energy resolution (up to $\sim$3.3 eV at 6.9 keV for our custom-designed BCLA for Ni, Cu and Zn spectral lines).

A four-element Vortex SDD, with each element 50 mm^2 active area, is also available from the APS detector pool. Two ion chambers located upstream and downstream of the KB mirrors' box, used for monitoring the flux of the incoming and delivered microbeam, complete the set of available detectors.

2.5. Fast-scanning XFM

XFM two-dimensional mapping experiments are performed by combining horizontal continuous scanning with vertical conventional step-mode scanning. Conventional two-dimensional mapping using step-scan mode, in both vertical and horizontal directions, is also available. In continuous-scan mode the sample is raster scanned while the full fluorescence spectrum and motor positioning for each pixel are recorded on-the-fly (acquisition time per pixel can be as short as 50 ms). A drawback of the continuous-scanning mode over the conventional step-scanning mode for XFM studies is how to accurately determine the actual position of the sample while it is in continuous motion. For that purpose, simultaneous acquisition of the motor encoder position during the scans ensures the correct assignment of pixel positioning.

The total scan time per line, typically between 5 and 10 s, depends on the number of pixels scanned that are defined by the size of the tissue section and level of resolution requested. Total time per area is then defined by the number of lines to be determined. Typically, a 100 $\times$ 100 pixel area can be scanned in just 8–9 min. A total time of 30 min is usually required to scan up to three different regions of interest per sample. This fast-scanning mode allows an average of 48 tissue sections per day to be measured. Scanning of multiple samples is performed in batch mode. During the batch scans there is no user intervention required. Experimental data for each sample are recorded in separate files. This allows users to gain immediate access to the data recorded while the system continues scanning the next sample in the batch.

Two DXP spectrometer units may be connected to the output of a single SDD in order to minimize the overhead time during the scanning process. When one spectrometer is acquiring the spectrum of a given pixel, the data from the previous pixel that was recorded in the other DXP unit is read out. As the scan advances to the next pixel the operation of the boxes is swapped, thus the one that was acquiring the data is now being read out while the other unit is taking new data from the new pixel position. Overhead time is minimized using this reading mode because the readout of a DXP unit and the motor encoder positions is carried out during the acquisition time of the other DXP unit. We have not observed any interference effect during the operation of two DXP units.

The collected full spectrum per pixel and its *XY* coordinate positions and other beamline parameters are stored in HDF5 file format, which offers a reliable and versatile format for large data sets storage. The HDF5 files can easily be accessed for XFM data analysis. During the data analysis process the measured pixel positions are used to construct a two-dimensional grid where the measured intensities are assigned. This simple procedure allows the images to be corrected for distortions in the distribution owing to the continuous-scan approach (see Fig. 5). Two analysis packages are currently available: BioCAT's *FMap* software (written in *Matlab*) for rapid data evaluation during the experiment and *MAPS* software (Vogt, 2003).

2.6. MicroXAS

MicroXAS scans are also performed in continuous-scan mode, with 15–30 s typical scan times using synchronous scanning of the undulator's gap and monochromator's energy. This scanning mode allows maximizing the beam intensity over the selected energy range. For even shorter scan times (5–10 s) the undulator is tapered to provide a wide energy range without being scanned, although the delivered intensity decreases compared with the synchronous scan mode. The combination of the upstream beam-defining slits and downstream aperture ensure a stable positioning of the focal spot during the energy scans. In this scanning mode the external output signal from a single DXP spectrometer is sent to a Struck Sis36/38 scaler that is recorded along with the encoder pulses from the monochromator positions on-the-fly. For microXAS measurements, *IFEFFIT* is the preferred analysis package (Ravel & Newville, 2005).

Although microXAS mapping experiments are feasible at BioCAT, they are not routinely performed owing to limited availability of beam time per experiment. Speciation mapping determinations are typically performed by measuring the fluorescence emission of the element of interest at selected excitation energies (Barrea, Chen *et al.*, 2009). The combina-

tion of the BioCAT microprobe control system and the fast-scanning capabilities of the beamline allow switching from XFM imaging experiments to microXAS measurements with minimal re-adjustments in reasonable time.

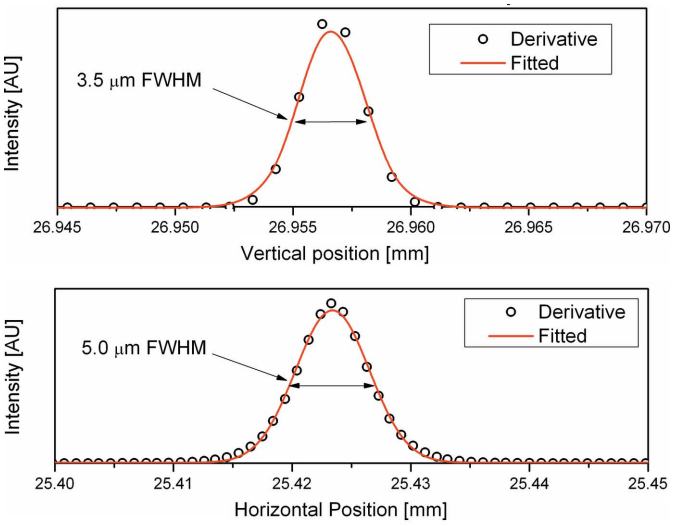

Figure 3
Vertical and horizontal beam profiles at 12 keV determined by knife-edge scan of a Ni thin film supported in a Si wafer. The fluorescence signal from the Ni film was measured using the continuous-scan mode. The recorded knife-edge data were fitted using a step function represented by the following equation: $y = A1 + (A2 - A1)/\{1 + 10^{[\log(x_0)-x]p}\}$, where $A1$ = bottom asymptote; $A2$ = top asymptote; $\log(x0)$ = center; and p = hill slope. The step-function fitted curve was then derived (represented by open circles in the graph) and finally a Gaussian function was used to find the FWHM value of the profile. In the case of the horizontal profile, the FWHM value is corrected considering the knife-edge scan is performed on a sample aligned at a 45° angle relative to the incoming beam. Similar results are obtained at 9.0 keV and 13.5 keV.

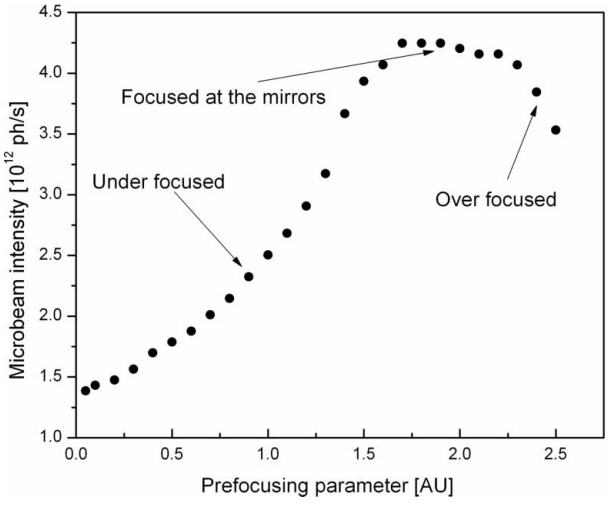

Figure 4
Microbeam flux delivered by the KB mirrors under prefocusing conditions in the horizontal direction. The intensity increases from 1.3×10^{12} photons s^{-1} as the beam is prefocused by the beamline main optics. The intensity achieves its maximum value of 4.2×10^{12} photons s^{-1} when the size of the prefocused beam equals the size acceptance aperture of the mirrors. Then the intensity decreases when the beam is over-focused and its size exceeds the mirror aperture.

3. Results

3.1. Focusing and prefocusing performance of the KB mirrors

The new KB bender system is highly reliable and allows precise selection of predetermined focusing configurations with very high reproducibility. Beam size may be rapidly and accurately changed between 100 μm, 20 μm to 3.5–5.0 μm FWHM in the vertical and horizontal directions, respectively. Fig. 3 shows vertical and horizontal beam profiles of a 12 keV focused beam determined by knife-edge scanning of a Ni thin film at the focal spot. The KB mirrors system delivers a microbeam flux of 1.3×10^{12} photons s^{-1} at 12 keV with similar results at 9 keV and 13.5 keV.

For higher flux delivery, we evaluated several prefocusing configurations including under-focused (virtual secondary source) and over-focused (real secondary source) conditions. A total flux of 4.2×10^{12} photons s^{-1} and 15 μm horizontal FWHM focal spot size was achieved by prefocusing the incident beam at the central position of the horizontal KB mirror (see Fig. 4). An additional two-fold increase in flux could be obtained by prefocusing the beam in the vertical direction, using the beamline bimorph mirror. This configuration requires large reconfiguration of the standard microprobe set-up to accommodate the change in beam angle. In practice, this effort is seldom justified. A theoretical evaluation of this configuration by phase space calculations and ray tracing along with additional experimental results can be found elsewhere (Huang *et al.*, 2010).

3.2. Fast-scanning performance

We have compared continuous-scans data with step-scans data taken from samples with known metal spatial distributions (Cu EM grid, T600H-Cu, 698 Hex mesh). We have observed no distortions to the real metal distribution in the sample obtained by continuous-scan determinations. Fig. 5 shows the Cu distributions obtained using conventional step scans and BioCAT's continuous scans, where the corrected

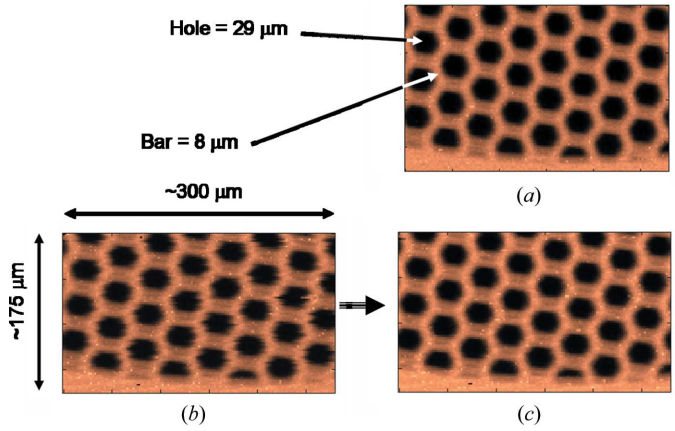

Figure 5
X-ray fluorescence map of the Cu EM grid. The 600 mesh T601H-Cu EM grid features are as follows: pitch = 32 μm; hole = 29 μm; bar = 8 μm. (*a*) Cu distribution obtained by step-mode scanning. (*b*) Cu distribution before corrections, obtained by continuous mode. (*c*) Corrected Cu distribution in continuous-scan mode.

distributions are also shown. As can be seen, the map obtained using continuous scanning, after the correction procedure, is indistinguishable from that obtained using conventional step scanning. The acquisition time for either step-scan mode or continuous-scan mode was 1.0 s pixel^{-1} or 0.1 s pixel^{-1}, respectively. Continuous scanning therefore results in a factor of ten increase in speed without reduction of data quality. It is worth mentioning here that in both scan modes the full spectrum per pixel is recorded; therefore no information is lost during continuous scanning. This feature becomes crucial when determining the content of trace elements whose spectral lines might overlap with other element lines also present in the sample.

3.3. Fast-scanning XFM of prostate tissue microarrays

Human tissue sections from many organs and different patients, histopathologically classified and prepared, are now commercially available as microarrays. These sets of arrayed samples in combination with the BioCAT fast-scanning microprobe provide an unprecedented opportunity for studies of metal distribution in relation to a wide variety of human diseases. We now present some initial results on elemental mapping from prostate tissue sections obtained from a tissue bank that have been studied using the microprobe in continuous-scan mode. Two sets of 24 sections each of normal and tumor prostate tissue array samples, purchased from BioMax, were studied by XFM. The arrays were mounted on ultralene thin film that is supported by an acrylic frame (BSL1 sample holders). The sample holder was initially mounted at the *XYZ* microprobe sample positioner in order to determine the areas to be scanned. The input parameters for each sample-scan are then recorded in an input data file in ASCII format using BioCAT's scan software. The scans were performed in batch mode.

Fig. 1 shows examples of elemental maps of Fe, Cu and Zn of prostate normal, hyperplasia and tumor tissue measured at 12 keV incident energy. Fig. 6 shows representative single-pixel and cumulative spectra. We found a large variability of metal content among specimens from different patients of a wide range of ages, making the evaluation of the total elemental content somewhat difficult. For instance, we have observed a large variability of Cu content in tumor tissues, from lower to higher accumulation compared with normal tissue values. When evaluating large data sets the main drawback is the normalization process. One can look at the relationship of Cu to Zn in another way that is independent of the absolute Zn or Cu contents by examining the Cu/Zn ratio. This can reduce bias owing to inhomogeneities in tissue thickness and other sources of variability. We have found that the Cu/Zn ratio observed in normal prostate tissue is altered in hyperplastic and tumor tissues. In hyperplastic tissue the Cu/Zn ratio alteration depends on the amount of additional accumulation of both ions, because pre-malignant cells tend to accumulate more Cu and Zn while in tumor tissue the level of Zn is slightly lower than in normal tissue, mainly because

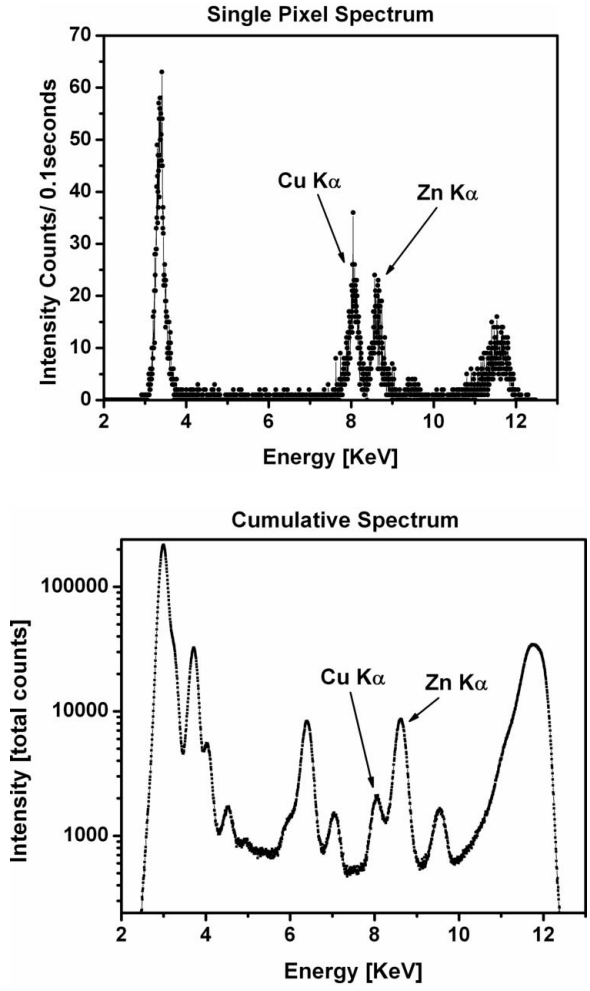

Figure 6
Representative fluorescence spectra. The single-pixel spectrum shows counts accumulated in 0.1 s exposure time. The cumulative spectrum is the sum of all spectra from the full sample area. It can be clearly seen that the cumulative spectrum shows fluorescence peaks of all elements present in the sample area while the single-pixel spectrum only shows those elements found in that particular pixel region. Also, it can be noticed that the Cu/Zn ratio in the single-pixel spectrum is not the same as the ratio in the cumulative spectrum representing the whole sample.

malignant cells lose their ability to accumulate more Zn (Ho & Song, 2009; Sapota *et al.*, 2009).

3.4. MicroXAS results on breast tissue sections

The alteration of the local content of metals in tumors compared with normal tissue may also be accompanied by modifications of their chemical environment. Cu, for instance, plays important roles in many different processes in human physiology. It is also known that Cu is involved in tumor growth and development. Cu has also been considered as a target for novel cancer therapies. When tumors are treated with certain copper chelators, such as disulfiram [DSF, a member of the dithiocarbamate family, an irreversible inhibitor of aldehyde dehydrogenase that binds to Cu(II)], they form copper complexes that inhibit proteasome activity and induce apoptotic cell death in tumor cells and xenographs (Chen *et al.*, 2006). The mechanism responsible for the DSF-

mediated antitumor activity has not been fully elucidated. In particular, the role of Cu in these processes is not completely understood. The distribution and quantity of Cu in DSF-treated tumor samples and controls can be addressed by microXANES measurements at the absorption edge of the element of interest (Cu *K*-edge in this case). Tissue sections from animal experiments in which human breast tumor xenografts were treated with DSF or the control solvent vehicle were studied by microXANES. Fig. 2 shows the measured Cu *K*-edge XANES spectra from untreated and DSF-treated tumor tissue sections. Each spectrum in Fig. 2 was obtained by repeating 100 times a single scan (~30 s per scan) in order to reduce the statistical errors below 5%, thus about 3000 s per spectrum/sample spot are required (beam size was 5 μm FWHM). Tumor tissue scans are compared with normal kidney and liver tissue from the same animal. The spectra show a predominant Cu(I) signal in all cases, although there is a slight difference observed at the pre-edge peak at 8930 eV. The observed Cu spectra in untreated tumor and normal liver and kidney tissue can be associated with three-coordinate Cu(I) complexes (Kau *et al.*, 1987). Liver and kidney tissues show no variations in their Cu spectral features after DSF treatment. On the other side, the peak intensity in DSF-treated tumor tissue sections is lower than in untreated tumor. This drop in intensity could be explained by a different three-coordinate Cu(I) environment, a change to a four-coordinated Cu(I) environment or by the contribution of a low concentration of a newly formed DSF–Cu(II) complex in tumor. These results suggest that copper has a unique chemical environment in tumor which may lead to its selective interaction of DSF with tumor and not with normal breast tissue or other normal tissues (liver and kidney). Additional details of this experiment can be found elsewhere (Barrea *et al.*, 2010).

4. Conclusion

The recently upgraded BioCAT X-ray microprobe is fully operational for biological XFM and microXAS applications. The new KB mirrors deliver a 1.3×10^{12} photons s^{-1} X-ray beam and they cover a wide range of easily selectable beam sizes, from 100 μm down to 5 μm FWHM. BioCAT's prefocusing capabilities allow further increasing up to three-fold the beam flux delivered with minimal set-up changes and slightly large beam size (~15 μm FWHM). BioCAT's continuous-scan software has been improved with providing a full MCA spectrum per pixel recorded on-the-fly. The typical acquisition time per pixel is ~100–50 ms. The total scan time is 8–9 min for the 100 × 100 pixels area and a total of 30 min per sample (up to six different regions of interest or at different resolution 20 μm to 5 μm). These upgrades allow the evaluation of up to 48 samples per day. Swapping between XFM and XAS experiments can be done with minimal set-up time (less than 30 min), allowing the end user to obtain elemental mapping and spectroscopy data during the same visit to BioCAT. X-ray fluorescence distributions taken under the continuous-scan mode of operation show the same high image quality compared with those obtained by step-scan mode. Data are recorded in HDF5 file format providing a reliable and easy mode of storing and handling large data sets. The microprobe is ready for BSL1 and BSL2 type experiments. Cryo-capabilities have also been incorporated in the microprobe, including a motorized cryostage. Two visualization software packages are available for in-house evaluation during the experiment and for complete and detailed analysis afterwards.

APPENDIX *A*
Companies selected to provide the main components of the microprobe

Linear stages from Newport Corp: http://www.newport.com/.
KB mirrors from University of Chicago: http://www.uchicago.edu/.
Cryostages from Linkam: http://www.linkam.co.uk/.
Light microscope from Edmund Optics: http://www.edmundoptics.com/.
Silicon drift detector from Ketek GmbH: http://www.ketek.net/.
File format from: http://www.hdfgroup.org/HDF5/.
Matlab platform: http://www.mathworks.com/.

BioCAT is a NIH-supported Research Center, RR08630. Use of the Advanced Photon Source was supported by the US Department of Energy, Basic Energy Science, Office of Energy Research, under Contract No. W-31-109-Eng-38. Project also supported by award number R21CA139386 from the National Cancer Institute. Dr Q. Ping Dou and Dr Di Chen (Karmanos Cancer Institute, Wayne State University, Detroit, MI, USA) are gratefully acknowledged for kindly providing breast tumor tissue and normal kidney and liver samples. The content is solely the responsibility of the authors and does not necessarily reflect the official views of the National Center for Research Resources or the National Institutes of Health.

References

Barrea, R. A., Chen, D., Irving, T. C. & Dou, Q. P. (2009). *J. Cell. Biochem.* **108**, 96–105.
Barrea, R. A., Chen, D., Irving, T. C. & Dou, Q. P. (2010). In preparation.
Barrea, R. A., Fischetti, R., Stepanov, S., Rosenbaum, G., Black, E., Gore, D., Heurich, R., Vukonich, M., Kondrashkina, E., Kropf, A. J., Wang, S., Zhang, K., Irving, T. C. & Bunker, G. B. (2005). *Phys. Scr.* T**115**, 867–869.
Barrea, R. A., Gore, D., Kondrashkina, E., Weng, T., Heurich, R., Vukonich, M., Orgel, J., Davidson, M., Collingwood, J. F., Mikhaylova, A. & Irving, T. C. (2006). *Proceedings of the 8th International Conference on X-ray Microscopy, IPAP Conference Series 7*, pp. 230–232.
Barrea, R. A., Huang, R., Cornaby, S., Bilderback, D. H. & Irving, T. C. (2009). *J. Synchrotron Rad.* **16**, 76–82.
Bohlen, A. von, Kramer, M., Hergenroder, R. & Berges, U. (2007). *AIP Conf. Proc.* **879**, 852–855.
Chen, D., Cui, Q. C., Yang, H. & Dou, Q. P. (2006). *Cancer Res.* **66**, 10425–10433.
Eng, P. J., Newville, M., Rivers, M. L. & Sutton, S. R. (1998). *Proc. SPIE*, **3449**, 145–156.

Farquharson, M. J., Geraki, K., Falkenberg, G., Leek, R. & Harris, A. (2007). *Appl. Radiat. Isotop.* **65**, 183–188.
Finney, L., Mandava, S., Ursos, L., Zhang, W., Rodi, D., Vogt, S., Legnini, D., Maser, J., Ikpatt, F., Olopade, O. I. & Glesne, D. (2007). *Proc. Natl. Acad. Sci. USA*, **104**, 2247–2252.
Fischetti, R., Stepanov, S., Rosenbaum, G., Barrea, R., Black, E., Gore, D., Heurich, R., Kondrashkina, E., Kropf, A. J., Wang, S., Zhang, K., Irving, T. C. & Bunker, G. B. (2004). *J. Synchrotron Rad.* **11**, 399–405.
Heald, S. M., Cross, J. O., Brewe, D. L. & Gordon, R. A. (2007). *Nucl. Instrum. Methods Phys. Res. A*, **582**, 215–217.
Ho, E. & Song, Y. (2009). *Curr. Opin. Clin. Nutr. Metab. Care*, **12**, 640–645.
Huang, R., Barrea, R. A., Irving, T. C. & Meron, M. (2010). *J. Synchrotron Rad.* Submitted.
Kau, L., Spira-Solomon, D., Penner-Hahn, J. E., Hodgson, K. O. & Solomon, E. I. (1987). *J. Am. Chem. Soc.* **109**, 6433–6442.
Kropf, A. J., Finch, R. J., Fortner, J. A., Aase, S., Karanfil, C., Segre, C. U., Terry, J., Bunker, G. & Chapman, L. D. (2003). *Rev. Sci. Instrum.* **74**, 4696–4702.
Kropf, A. J., Fortner, J. A., Finch, R. J., Cunnane, J. C. & Karanfil, C. (2005). *Phys. Scr.* T**115**, 998–1000.
Marcus, M. A., MacDowell, A. A., Celestre, R., Manceau, A., Miller, T., Padmore, H. A. & Sublett, R. E. (2004). *J. Synchrotron Rad.* **11**, 239–247.
Paterson, D. J., Boldeman, J. W., Cohen, D. D. & Ryan, C. G. (2007). *AIP Conf. Proc.* **879**, 864–867.
Paunesku, T., Vogt, S., Irving, T. C., Lai, B., Barrea, R. A., Maser, J. & Woloschak, G. E. (2009). *Int. J. Radiat. Biol.* **85**, 710–713.
Paunesku, T., Vogt, S., Maser, J., Lai, B. & Woloschak, G. E. (2006). *J. Cell. Biochem.* **99**, 1489–1502.
Ravel, B. & Newville, M. (2005). *J. Synchrotron Rad.* **12**, 537–541.
Sapota, A., Darago, A., Taczalski, J. & Kilanowicz, A. (2009). *Biometals*, **22**, 1041–1049.
Somogyi, A., Tucoulou, R., Martinez-Criado, G., Homs, A., Cauzid, J., Bleuet, P., Bohic, S. & Simionovici, A. (2005). *J. Synchrotron Rad.* **12**, 208–215.
Susini, J., Salome, M., Fayard, B., Ortega, R. & Kaulich, B. (2002). *Surface Rev. Lett.* **9**, 203–211.
Suzuki, Y., Takeuchi, A. & Terada, Y. (2007). *Rev. Sci. Instrum.* **78**, 053713.
Vogt, S. (2003). *J Phys IV*, **104**, 635–638.
Zhong, Z., Chapman, L. D., Bunker, B. A., Bunker, G., Fischetti, R. & Segre, C. U. (1999). *J. Synchrotron Rad.* **6**, 212–214.